

Atmospheric Temporal Variations in The Pre-Landfall Environment of Typhoon Nangka (2015) Observed by The Himawari-8 AHI

Yong-Keun Lee¹, Jun Li¹, Zhenglong Li¹, and Timothy Schmit²

¹Cooperative Institute for Meteorological Satellite Studies, University of Wisconsin-Madison, Madison, WI, USA

²Center for Satellite Applications and Research, NESDIS/NOAA, Madison, WI, USA

(Manuscript received 1 December 2016; accepted 27 March 2017)

© The Korean Meteorological Society and Springer 2017

Abstract: The next generation Geostationary Operational Environmental Satellite-R series (GOES-R) Advanced Baseline Imager (ABI) legacy atmospheric profile (LAP) retrieval algorithm is applied to the Advanced Himawari Imager (AHI) radiance measurements from the Himawari-8 satellite. Derived products included atmospheric temperature/moisture profiles, total precipitable water (TPW), and atmospheric stability indices. Since both AHI and ABI have 9 similar infrared bands, the GOES-R ABI LAP retrieval algorithm can be applied to the AHI measurements with minimal modifications. With the capability of frequent (10-min interval) full disk observations over the East Asia and Western Pacific regions, the AHI measurements are used to investigate the atmospheric temporal variation in the pre-landfall environment for typhoon Nangka (2015). Before its landfall over Japan, heavy rainfalls from Nangka occurred over the southern region of Honshu Island. During the pre-landfall period, the trends of the AHI LAP products indicated the development of the atmospheric environment favorable for heavy rainfall. Even though, the AHI LAP products are generated only in the clear skies, the 10-minute interval AHI measurements provide detailed information on the pre-landfall environment for typhoon Nangka. This study shows the capability of the AHI radiance measurements, together with the derived products, for depicting the detailed temporal features of the pre-landfall environment of a typhoon, which may also be possible for hurricanes and storms with ABI on the GOES-R satellite.

Key words: Advanced Baseline Imager (ABI), Advanced Himawari Imager (AHI), typhoon Nangka, LAP retrieval

1. Introduction

The next generation Geostationary Operational Environmental Satellite series (GOES-R) satellite was launched on 19 November, 2016 with several instruments including the Advanced Baseline Imager (ABI) (Schmit et al., 2005, 2017). ABI will provide 25 meteorological and/or environmental products. Although, there have been several validation studies for the ABI products using instruments such as the Spinning Enhanced Visible and Infrared Imager (SEVIRI) (Jin et al., 2008) and the Geostationary Operational Environmental Satellite (GOES) sounder (Lee et al., 2014), the best proxy mea-

surements are from Himawari-8, the Japanese geostationary meteorological satellite launched on 7 October, 2014. The main earth-viewing sensor of Himawari-8 is the Advanced Himawari Imager (AHI), which enables enhanced weather monitoring, numerical weather prediction and environment monitoring (Bessho et al., 2016). According to Padula and Cao (2014), the effective temperature difference between AHI and ABI is within 1 K for the infrared bands. 15 bands (out of the 16 bands) on the AHI and ABI are spectrally similar, with the main difference being a visible band that's on the ABI, and a near-IR band on the AHI. The number of spectral bands and the frequency of measurements of these two instruments are significant improvements compared to those of the heritage instruments, the GOES imager and the Multifunction Transport Satellite (MTSAT)-2 imager (Schmit et al., 2005; http://www.data.jma.go.jp/mscweb/en/himawari89/space_segment/spsg_ahi.html), respectively. Since the GOES-R ABI legacy atmospheric profile (LAP) retrieval algorithm is based on the infrared bands (Li et al., 2010; Lee et al., 2014), and both AHI and ABI have the similar 9 infrared bands, the GOES-R ABI LAP algorithm can be applied to the AHI measurements with minimal modifications. Currently, AHI provides full disk image every 10 minutes with 2-km horizontal resolution over the East Asia and Western Pacific regions centered at the longitude of 140.7°E (<https://directory.eoportal.org/web/eoportal/satellite-missions/h/himawari-8-9#S1If112eHerb>). The observation frequency of 10 minutes is critical to weather monitoring because there could be significant changes in the atmosphere, even in a 10-min interval. Schmit et al. (2013, 2015) showed that super rapid scan operations for GOES-R (SRSOR) using the GOES-14 imager can observe the movement or development of clouds, convection, severe storms, tropical cyclones and so on even in 1-min mode. Since the MTSAT-2 imager and the GOES imager generate a full disk image every 30 minutes, the more frequent observations will allow monitoring more detailed temporal changes of the atmosphere. Furthermore, the AHI measurements can be used to retrieve the atmospheric temperature/moisture profiles, total precipitable water (TPW), and the atmospheric stability indices, similar to the ABI which will provide the heritage legacy products of the current GOES sounder (Schmit et al., 2008). With the capability of retrieving the legacy products, the observation frequency (10 minutes for

Corresponding Author: Yong-Keun Lee, CIMSS, University of Wisconsin, 1225 West Dayton St., Madison, WI 53706, USA.
E-mail: yklee@ssec.wisc.edu

the full disk) of AHI will provide unprecedented opportunities for high temporal weather and environmental monitoring. Even though the retrieval is valid over clear skies, the variation of the atmospheric stability may provide useful information on whether the environment is favorable for convection (Li et al., 2011, 2012; Lee et al., 2014). This research is a case study regarding the pre-landfall environment over Japan for typhoon Nangka (2015) by applying the GOES-R ABI LAP retrieval algorithm (Jin et al., 2008; Lee et al., 2014) to the high temporal AHI full disk measurements (termed the AHI LAP retrieval algorithm).

A brief description about the AHI measurements, the AHI LAP retrieval algorithm and the reference data are provided in Section 2. Section 3 describes the results and the discussion of the AHI LAP products, while a summary is given in Section 4.

2. The AHI LAP retrieval algorithm and the reference data

a. The AHI data and the AHI LAP retrieval algorithm

AHI on board Himawari-8 has 16 bands including 9 infrared bands longer than $6\ \mu\text{m}$ (these are not affected by solar contamination) in wavelength (similar to ABI) and 8 infrared bands are used in the AHI LAP retrieval algorithm except the ozone band (band 12, centered at $9.6\ \mu\text{m}$). AHI provides brightness temperatures (BTs) over full disk every 10 minutes with 2-km horizontal resolution at the sub-point, which would be a possible scan plan for the GOES-R ABI. Table 1 shows the wavelength and its usage in the LAP algorithm of each AHI infrared band.

The AHI LAP retrieval algorithm is based on the GOES-R ABI LAP retrieval. The algorithm includes regression and physical retrieval processes with the most recent National Centers for Environmental Prediction (NCEP) Global Forecast System (GFS) forecast data as the background in the regression step. The regression coefficients are generated based on the global profile training database, the SeeBor database (Seemann et al., 2003, 2008), which has been used as training dataset for many sounding applications (e.g., Lee et al., 2014). Only profiles that match the Himawari-8 AHI disk observation coverage are used. The NCEP GFS 3-, 6-, 9-, 12-hr forecast fields are available every 6 hours (0000, 0600, 1200, 1800 UTC) over the globe at 0.5° horizontal resolution with 26 vertical levels. They are spatially and temporally interpolated to the AHI measurement grids and to 101 vertical pressure levels. The Community Radiative Transfer Model (CRTM, version 2.0.2) developed by the National Oceanic and Atmospheric Administration (NOAA)'s Joint Center for Satellite Data Assimilation (JCSDA) is used to simulate the AHI BTs and calculate the Jacobian (Weng et al., 2005; Chen et al., 2010, 2012). To speed up the process, the retrievals are performed on a 5×5 pixel block instead of every pixel. This is equivalent to reduce the AHI's spatial resolution to 10 km. However, as presented in this study, even with the resolution of

Table 1. AHI Bands used for the AHI LAP algorithm (<https://directory.eoportal.org/web/eoportal/satellite-missions/h/himawari-8-9/#S1It12eHerb> for AHI, and Lindsey et al. (2012) for ABI).

Band Number	Wavelength (μm)	Purpose
8	6.19 (6.19: ABI)	High-level atmospheric water vapor, winds, rainfall
9	6.95 (6.93: ABI)	Mid-level atmospheric water vapor, winds, rainfall
10	7.34 (7.34: ABI)	Lower-level atmospheric water vapor, winds, and SO_2
11	8.50 (8.50: ABI)	Total water for stability, cloud phase, dust, SO_2 , rainfall
13	10.35 (10.33: ABI)	Surface and cloud
14	11.20 (11.20: ABI)	Imagery, Sea Surface Temperature (SST), clouds, rainfall
15	12.30 (12.30: ABI)	Total water, ash, Sea Surface Temperature (SST)
16	13.30 (13.30: ABI)	Air temperature, cloud heights and amounts

10 km, AHI is capable of providing useful information on the pre-landfall environment of typhoon Nangka. Another advantage of this is the reduced observation noise and cloud contamination from the average of all clear sky pixels among 5×5 AHI block. The retrieval is performed when the number of clear pixels is above or equal to 20 (or 80% of the pixels) or more are clear among the total 25 pixels. Currently a simple cloud detection algorithm is used, which is based on the BT difference at $13.3\ \mu\text{m}$ between the observed and the calculated using a clear sky model; differences larger than 2 K are considered cloud contaminated. The explicitly determined 2-K criterion is very effective to detect cloudy pixels. As a matter of fact, it is so strict that it might misclassify a clear pixel as cloudy. This might lose some clear sky pixels, but significantly reduce the possibility of cloud contamination. The operational GOES-R ABI LAP algorithm uses the operational ABI cloud mask to detect cloudy pixels. The details of the GOES-R ABI LAP algorithm can be found at Jin et al. (2008) and Lee et al. (2014).

b. The integrated surface data and ECMWF analysis

The Integrated Surface Data (ISD) database integrates global hourly and synoptic observations from over 100 sources into a unified ASCII format. The database includes over 35,000 global stations with the precipitation amounts for various time periods. ISD and the related documents are available at <http://www.ncdc.noaa.gov/>. To investigate the pre-landfall environment of typhoon Nangka, 11 ISD stations over Japan area (southern region of Honshu Island) have been selected where the observed accumulated rainfall was more than 30 mm on 15 July and 100 mm over the two days, 15 and 16 July. The rainfall occurred mostly after 1200 UTC on 15 July and the

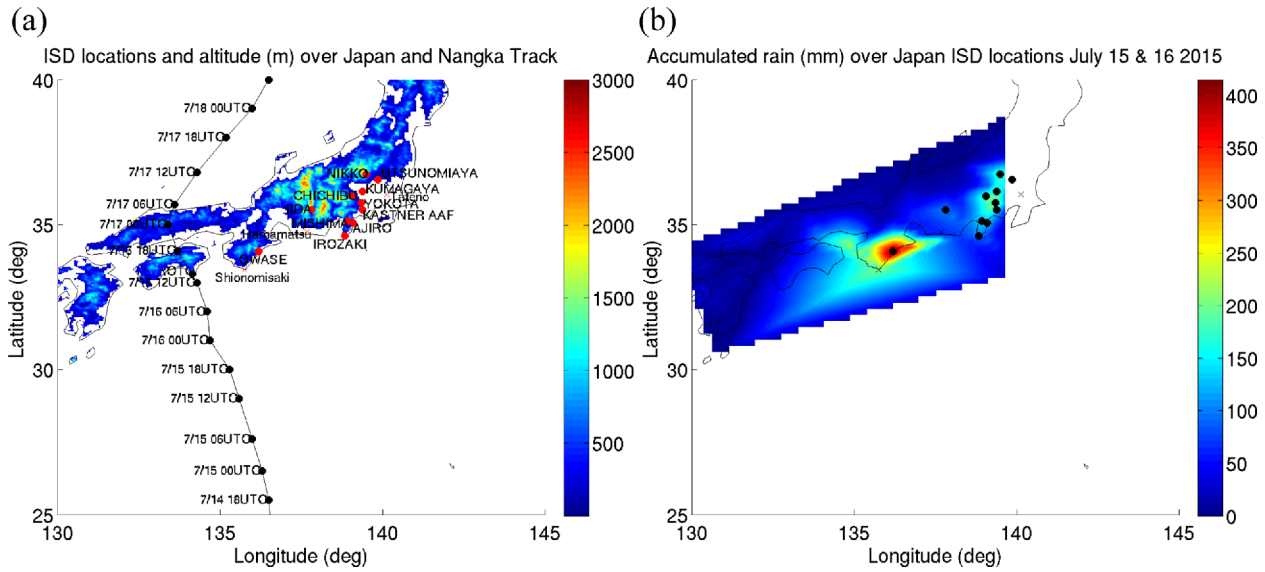


Fig. 1. (a) ISD locations over Japan where the accumulated rainfall was over 30 mm in 15 July, 2015 and over 100 mm during two days in 15 and 16 July, 2015. The track of typhoon Nangka (JMA) and elevation are also shown. (b) Accumulated rainfalls during 15 and 16 July, 2015 are shown. Accumulated rainfalls are interpolated from each site's rainfall information (including the sites where small amount of precipitation has been observed). Three locations of "x" in (a) and (b) are the radiosonde sites providing atmospheric stability indices and TPW during the same period.

accumulated amount is more than 50 mm on 16 July according to the ISD observations at 11 locations. After 16 July, the rainfall amounts decreased significantly over these locations (not shown). The 6- or 12-hr accumulated rainfalls at these 11 ISD stations are shown in Table 2 and the locations of these stations are shown in Fig. 1a. Since the AHI LAP retrieved outputs are generated at 10 km resolution, the closest block are searched for each 11 ISD stations within 7 km.

The European Centre for Medium-Range Weather Forecasts (ECMWF) provides global atmospheric analysis data every 6 hours with a spatial resolution of 0.25 degree in latitude/longitude and with 91 vertical pressure levels. The ECMWF analysis data are interpolated to match the AHI measurements and used as reference to show the overall quality of the AHI LAP retrievals. Note that the ECMWF forecast does not assimilate the AHI measurements (<http://www.ecmwf.int/sites/default/files/elibrary/2016/16646-part-i-observations.pdf>).

3. Results and discussion

a. Synoptic environment

The synoptic conditions (500 hPa geopotential height and wind, mean sea level pressure and 10 m wind: ECMWF) are shown at 0000 UTC 15 July, 2015 in Figs. 2a and 2b. Typhoon Nangka is located at approximately 26.5°N and 136°E and the spiral shape of BT near the eye at 11.2 μm is evident in Fig. 2c. Typhoon Nangka moves northward around the western edge of the high pressure system located over the West Pacific area (centered at around 30°N and 160°E). A slowly eastward

moving low pressure system is centered at around Sakhalin Island (northeastern area in Figs. 2a and 2b). According to the storm advisory from the Joint Typhoon Warning Center (JTWC), convective development is inhibited due to the dry air and subsidence to the north and west providing the environment for typhoon Nangka to weaken (<http://www.webcitation.org/6a1ZNe1Ox>).

The orographic effect on the heavy rainfall has not been considered in this study. However, it is well known that the terrain may affect the precipitation amount (e.g., Lin et al., 2001). Many of the 11 ISD sites are located in the upslope region since southeasterly winds develop by the approaching typhoon (Figs. 1a and 2) where upslope and upstream triggering of convection would be possible (Houze, 1993). The accumulated rainfall amount has been drawn by the interpolation of each site's information (Fig. 1b). Considering the distribution of accumulated rainfall amount in Fig. 1b, the heavy rainfall is possibly related with the orographic effect and it would be interesting to see the terrain impacts on the precipitation in the future.

Typhoon Nangka was initiated by a tropical depression over the Marshall islands on 3 July, 2015 and experienced several fluctuations in its strength while moving westward before its landing over Japan according to the JTWC and the Japan Meteorological Agency (JMA). Typhoon Nangka made its first landfall over Muroto, Kochi of Japan at 1407 UTC 16 July, 2015. Even before its landfall, typhoon Nangka produced heavy rainfall over the south region of Honshu Island, mostly the right side of the track including the 11 ISD locations and the northern parts of the Greater Tokyo area in Fig. 1, meanwhile

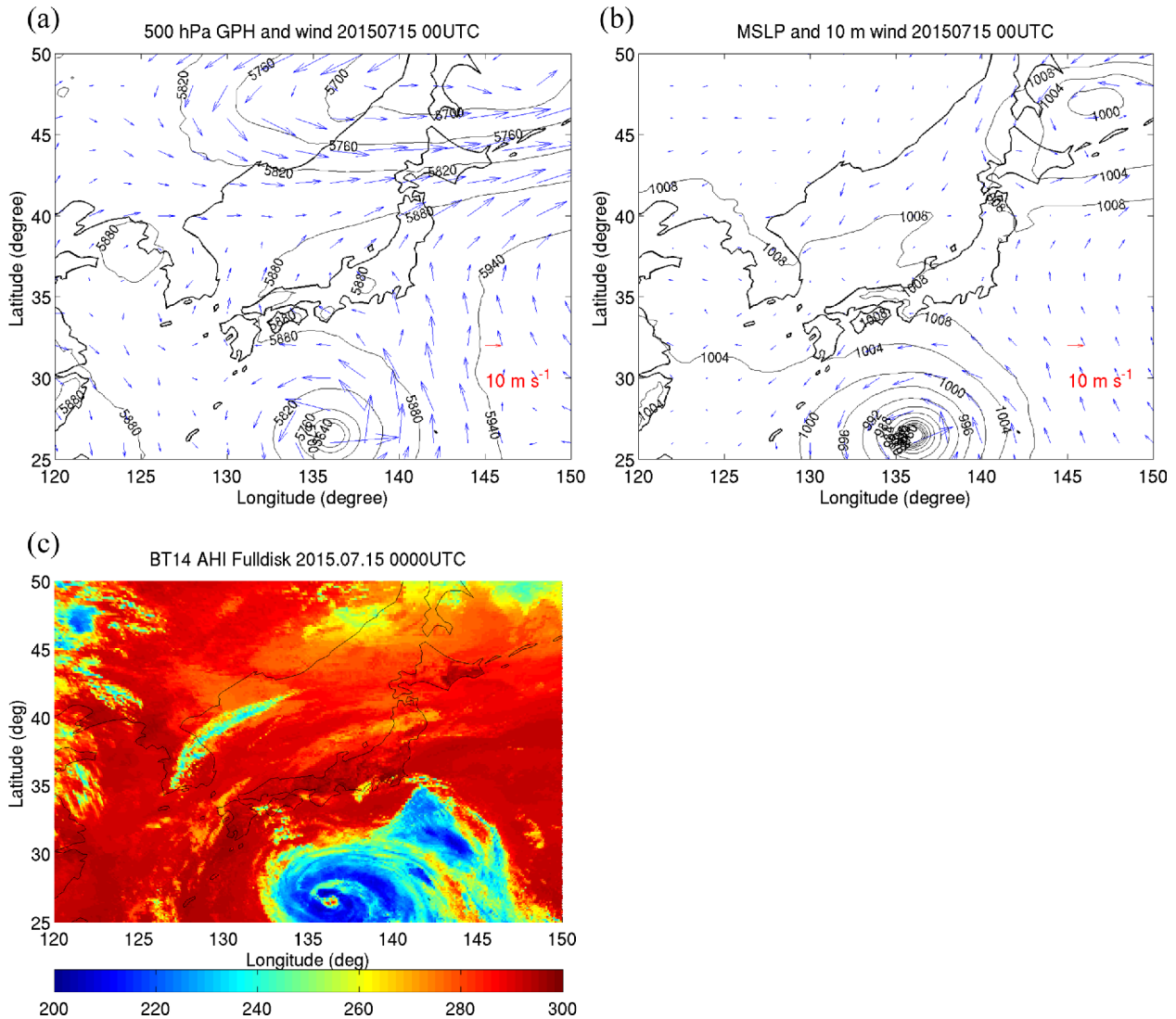


Fig. 2. (a) 500-hPa geopotential height (m) and wind (m s^{-1}) and (b) mean sea level pressure (hPa) and 10-m wind (m s^{-1}) from ECMWF analysis and (c) window band ($11.2 \mu\text{m}$) brightness temperature from AHI at 0000 UTC 15 July, 2015 (subsampled from the full disk observations).

typhoon Nangka was weakening during its passage over Japan.

Clouds begin to cover Japan due to the coming typhoon at around 0600 UTC 15 July, 2015. Since the AHI LAP retrieval algorithm is applied to the clear skies only and most of the pixels are cloudy in the later period, the atmospheric variation is investigated over the clear skies during the period between 1200 UTC 14 July and 0600 UTC 15 July. Among 11 ISD stations, Owase (34.07°N , 136.20°W) shows the maximum rainfall amount of 454 mm in Japan area during the two days, 15 and 16 July, according to the ISD database (Table 2). The 12-hr accumulated rainfall is 4 mm at 1200 UTC 15 July and increases to 114 mm at 0000 UTC 16 July over Owase.

b. AHI LAP retrievals

Figure 3 shows the bias and the standard deviation of the

AHI retrieved vertical temperature/moisture profiles compared with the ECMWF analysis data at 0000 UTC 15 July, 2015 for the AHI full disk and local area ($25\text{--}50^\circ\text{N}$, $120\text{--}150^\circ\text{E}$: around Japan), with a total number of clear sky pixels of 384,102 and 29,131, respectively. The bias and the standard deviation of the temperature and moisture (in relative humidity) profiles are similar over the full disk and local area. The temperature bias is smaller than 1 K in absolute value below 300 hPa and becomes larger in the upper atmosphere. The temperature standard deviation (STD) is smaller than 1 K throughout the troposphere and slightly larger than 1 K near 100 hPa. The comparison of water vapor shows (in relative humidity) larger bias in the upper and the lower troposphere where the AHI three water vapor absorption bands do not cover (i.e., the AHI three water vapor bands have weighting functions in the middle troposphere). The water vapor STD shows a consistent

Table 2. Accumulated rainfall (mm) over 11 stations in Japan during 15 and 16 July, 2015 from the ISD database. 12-hr accumulated rainfall is shown at 0000 and 1200 UTC and 6-hr accumulated rainfall is shown at 0600 and 1800 UTC except Kastner AAF. Note that the rainfall amount observed at 0000 UTC 17 July is for 16 July.

	15 July			16 July			17 July	
	0600 UTC (6 hrs)	1200 UTC (12 hrs)	1800 UTC (6 hrs)	0000 UTC (12 hrs)	0600 UTC (6 hrs)	1200 UTC (12 hrs)	1800 UTC (6 hrs)	0000 UTC (12 hrs)
Utsunomiya	0.0	0.0	4.0	77.0	57.0	64.0	4.0	4.0
Kumagaya	0.0	0.0	9.0	116.0	39.0	41.0	7.0	7.0
Iida	0.0	0.0	3.0	37.0	19.0	27.0	15.0	36.0
Chichibu	0.0	0.0	3.0	74.0	52.0	90.0	9.0	20.0
Yokota	0.0	0.0	3.4	107.7	82.2	82.9	39.5	40.8
Mishima	1.0	1.0	9.0	87.0	8.0	20.0	14.0	30.0
Owase	0.0	4.0	73.0	114.0	3.0	76.0	107.0	260.0
Irozaki	1.0	1.0	44.0	53.0	0.0	19.0	0.5	28.0
Ajiro	0.0	0.0	20.0	74.0	14.0	16.0	24.0	40.0
Kastner AAF	0.0	0.0	0.0	69.0 (6 hrs)	25.1	0.0	0.0	38.3 (6 hrs)
Nikko	0.0	0.0	8.0	68.0	44.0	64.0	44.0	54.0

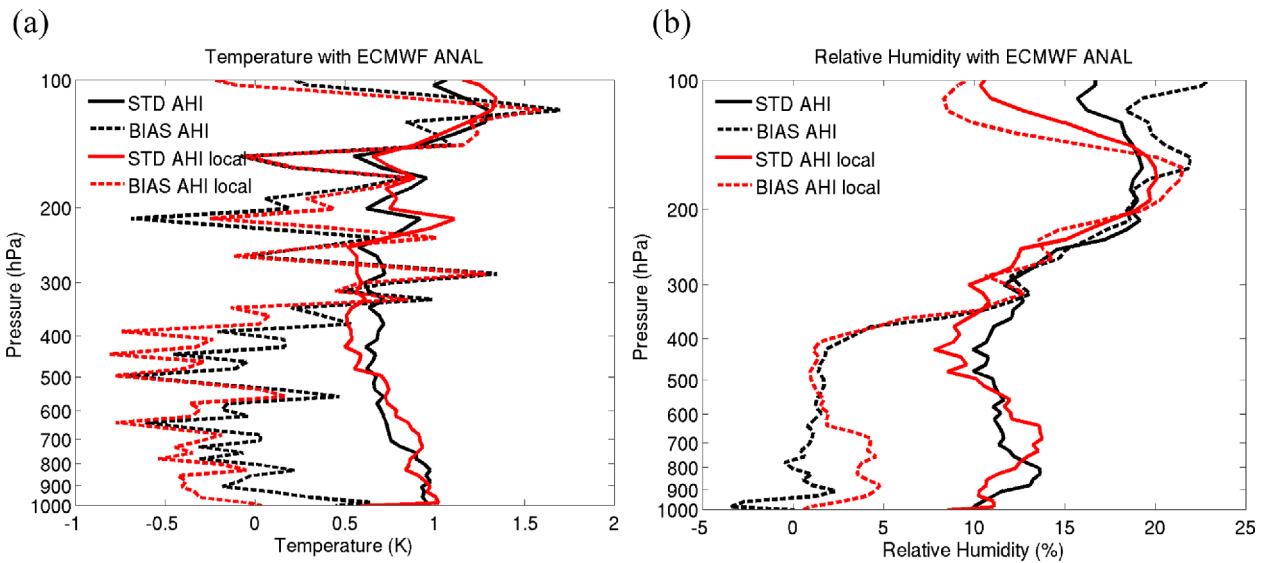


Fig. 3. The comparison of (a) temperature profiles and (b) water vapor (relative humidity) profiles retrieved from AHI LAP algorithm with the ECMWF analysis over the AHI full disk and local (25-50°N, 120-150°E) area at 0000 UTC 15 July, 2015.

performance throughout the troposphere with values between 10-20%. Both temperature and water vapor comparisons reveal that they are overall within the accuracy and precision requirement of the GOES-R ABI LAP outputs (Li et al., 2010). The GOES-R ABI LAP requirement is that the accuracy (precision) of temperature is 1 K (2 K) below 400 hPa and above boundary layer and the accuracy and the precision of water vapor are “18% between surface and 300 hPa” and “20% between 300 and 100 hPa” in relative humidity.

Atmospheric stability indices and TPW averaged over 11 ISD locations in the south region of Honshu Island are shown in the left column of Fig. 4 with 1-hr interval between 1200

UTC 14 July and 0600 UTC 15 July. Since the AHI measurements are available with the 10-min interval, the 10-min results are also included in the right column between 2200 UTC 14 July and 0300 UTC 15 July to highlight the short-term variation of the atmospheric state. The National Weather Service (NWS) has provided guidance (Table 3) on how to interpret various atmospheric stability indices. Lifted Index (LI) [T500-Tp500] is calculated using the hypothetical parcel being lifted dry adiabatically from the surface (with the mean layer value of temperature and water vapor in the lowest 100 hPa of the atmosphere) to the Lifted Condensation Level (LCL) and pseudo-adiabatically to 500 hPa and the tempera-

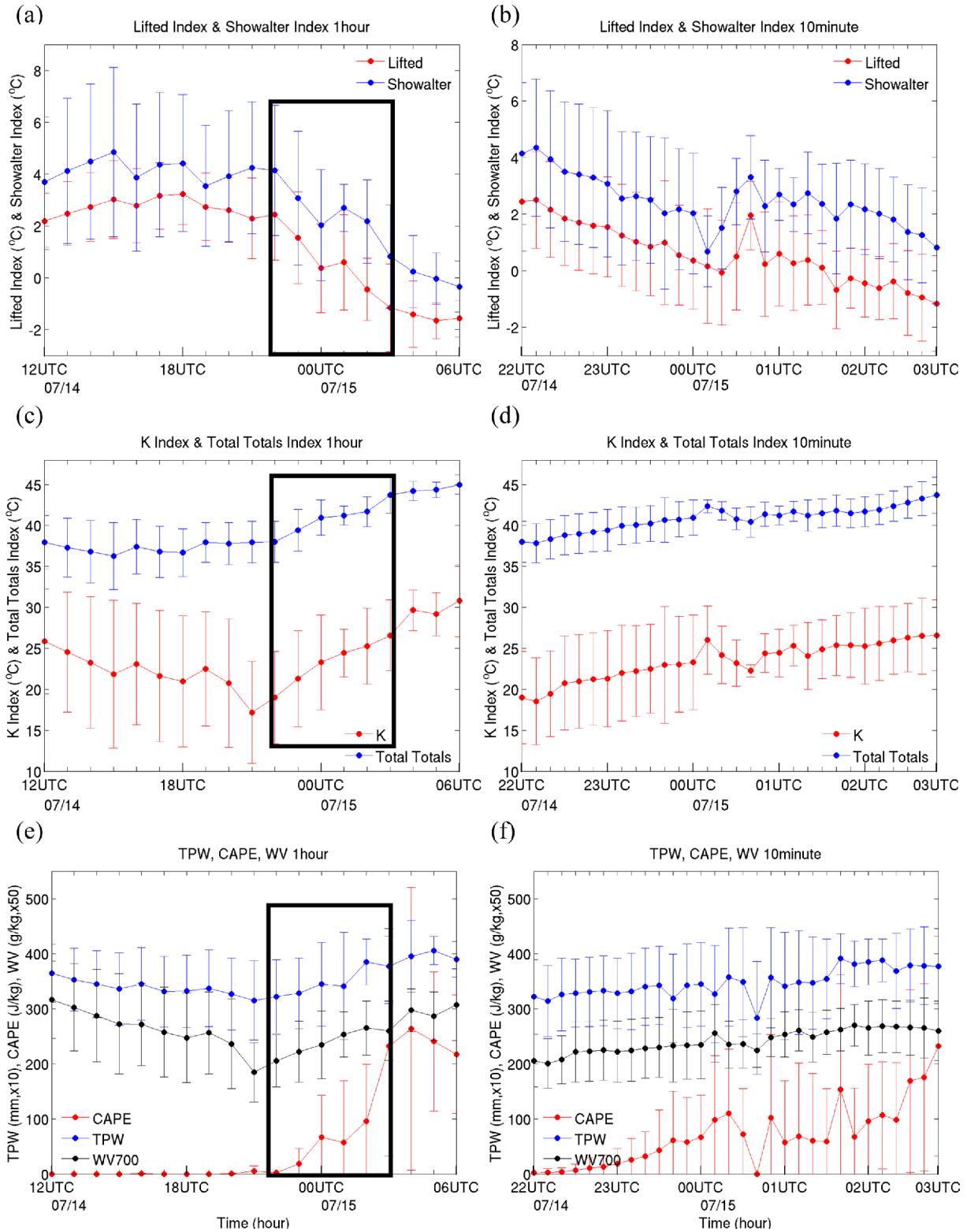


Fig. 4. Time series of the averaged TPW and atmospheric stability indices over 11 ISD locations in Japan where the accumulated rainfall was over 30 mm in 15 July, 2015 and over 100 mm during two days in 15 and 16 July, 2015. The left-hand side panels show the results with 1- hr interval between 1200 UTC 14 July and 0600 UTC 15 July and the right-hand side panels with 10-min interval between 2200 UTC 14 July and 0300 UTC 15 July (data missing at 0240 UTC 15 July). The rectangular boxes in the left-hand panels indicate the 10-min period in the right panels. (a) and (b) Lifted index and Showalter index, (c) and (d) K index and Total Totals index, and (e) and (f) TPW, CAPE and water vapor at 700 hPa (TPW and water vapor values are multiplied by 10 and 50, respectively). Vertical bars indicate the standard deviation over the selected 11 ISD locations.

Table 3. Atmospheric stability indices from the National Weather Service (NWS)'s guide (<http://weather.gov/ffc/gloss2>).

Atmospheric stability indices	Value range	Risk of thunderstorms and severe weather activity
Lifted index (°C)	LI > 2	No significant activity
	0 < LI < 2	Showers/thunderstorms possible with other source of lift
	-2 < LI < 0	Thunderstorms possible
	-4 < LI < -2	Thunderstorms more probable, but few, if any severe
	LI < -4	Severe thunderstorms possible
Showalter index (°C)	SI > 3	No significant activity
	1 < SI < 3	Showers possible with other source of lift
	-2 < SI < 1	Thunderstorms possible (generally weak)
	-3 < SI < -2	Thunderstorms more possible (possibly strong)
	-6 < SI < -4	Strong or severe thunderstorms possible
Total Totals Index (°C)	SI < -6	Any thunderstorms likely to be strong or severe
	44-45	Isolated moderate thunderstorms
	46-47	Scattered moderate/few heavy thunderstorms
	48-49	Scattered moderate/few heavy/isolated severe thunderstorms
	50-51	Scattered heavy/few severe thunderstorms and isolated tornadoes
	52-55	Scattered to numerous heavy/few to scattered severe thunderstorms/few tornadoes
K index (°C)	TT > 55	Numerous heavy/scattered severe thunderstorms and scattered tornadoes
	KI < 15	Near 0% air mass thunderstorm probability
	15-20	< 20% air mass thunderstorm probability
	21-25	20-40% air mass thunderstorm probability
	26-30	40-60% air mass thunderstorm probability
	31-35	60-80% air mass thunderstorm probability
	36-40	80-90% air mass thunderstorm probability
KI > 40	> 90% air mass thunderstorm probability	
CAPE (J kg ⁻¹)	CAPE < 1000	Weak instability
	1000 < CAPE < 2500	Moderate instability
	CAPE > 2500	Strong instability

ture of the environment (T500) is subtracted by the temperature of the parcel (Tp500) at 500 hPa, while Showalter Index (SI) [T500-Tp500_850] is similar to LI in calculation except the initial position of the hypothetical parcel is 850 hPa instead of the surface. Tp500_850 is the temperature of the parcel would have after being lifted to 500 hPa. K Index (KI) is calculated as $T850 - T500 + Td850 - (T700 - Td700)$ and Total Totals index (TT) as $T850 + Td850 - 2 * T500$, where T850 and Td850 are temperature and dew point temperature, respectively, at 850 hPa. Their difference is whether to take into account the moist air at 700 hPa contributing to air mass thunderstorm development. The Convective Available Potential Energy (CAPE) is a measure of the integrated buoyancy of a rising parcel from the level of free convection to the equilibrium level. The CAPE is calculated by the equation, $CAPE = g \int_{Z_f}^{Z_e} \frac{1}{T_{vb}} (T_{va} - T_{ve}) dz$, where Z_e is the equilibrium level, Z_f is the level of free convection, T_{va} and T_{ve} are wet-bulb potential temperature for the air parcel and the environment.

According to Masunaga (2012)'s study, the atmospheric

vertical structures (temperature/moisture) in a convective environment could be different between climate regimes. Considering that this study used the atmospheric stability indices categorized by the risk of thunderstorm probability as stated in the National Weather Service (NWS) guide, we might need to re-classify the probability of the atmospheric instability for each stability index for different climate regimes. However, since we are going to focus more on temporal variations or trend instead of individual snapshot values of these indices, no attempt will be performed to re-classify the probabilities of each index. The individual values will be interpreted in a qualitative manner.

Note that the atmospheric stability indices used in this study have been developed based on the observation over Continental United States (CONUS), which may have regional limitation in their application. In fact, many studies have applied these traditional atmospheric stability indices over the areas outside the CONUS region. For example, Huntreser et al. (1997) developed their own atmospheric stability indices

which show better predictability of thunderstorms than the traditional indices over Switzerland. Jayakrishnan and Babu (2014) also utilized the traditional atmospheric stability indices over India region with encouraging results; however, they indicated that the re-classification of the criteria of the stability indices might be needed over India. Again, since the traditional atmospheric stability indices have been developed based on the radiosonde data over the CONUS region, the application of these indices to other areas could be limited due to the differences in atmospheric and geographical characteristics between different regions over the globe. Some conditions favorable for development of the thunderstorms over CONUS may be summarized (Miller, 1972) as: 1) conditionally unstable thermal air structure: e.g. cooling of middle and higher levels and increase of surface temperature, 2) low level tongue of moisture and drier air above this ridge, 3) strong mid-level winds and sharp horizontal wind shears, 4) lifting mechanisms of different types of fronts, and several more. While the precipitation case considered in the current study was affected by a typhoon which has different atmospheric features compared to the thunderstorms over CONUS. Strong and deep convective clouds and nearly symmetric cyclonic flows centered at its eye with significant amount of water vapor from the ocean are the features of a typhoon. The precipitation in this study was caused by typhoon Nangka (2015) due to its enhanced northward moisture transport because of its outer circulation. Considering the atmospheric and geographic differences between CONUS and Japan area, the quantitative consideration of the traditional atmospheric stability indices of NWS could be limited over Japan.

All the averaged atmospheric stability indices imply the stable or relatively stable state during the first several hours after 1200 UTC 14 July and most of them show changes towards the unstable status quickly from around 2200 UTC 14 July. The hourly and 10-min variation of the atmospheric stability indices averaged over 11 ISD locations during this period shows the following features.

LI is above 2°C (no significant activity) between 1200 UTC and 2200 UTC 14 July and becomes negative (thunderstorms possible) at 0200 UTC 15 July in Fig. 4a. SI is above 3°C (no significant activity) between 1200 UTC and 2300 UTC 14 July and becomes less than 1°C (thunderstorms possible: generally weak) at 0300 UTC 15 July in Fig. 4a. The 10-min interval variations of both LI and SI show decreasing trend between 2200 UTC 14 July and 0300 UTC 15 July in Fig. 4b, although there are some increases in LI and SI between 0020 UTC and 0040 UTC July 15 which are shown as weaker increases in the 1-hr frequency. These increases are corresponding to the decrease of water vapor in the lower atmosphere below 700 hPa during this time period (Fig. 4f). LI becomes negative at 0140 UTC 15 July and SI becomes less than 1°C at 0300 UTC 15 July in Fig. 4b. Due to the similarity of the calculation between LI and SI, their trends are highly correlated in this study: their correlation coefficients are 0.97 for the 1-hr interval trend (Fig. 4a) and 0.88 for the 10-min interval trend

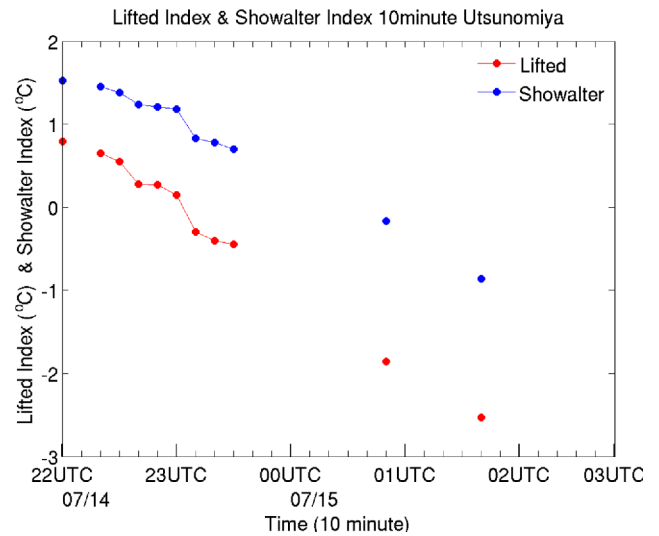


Fig. 5. Time series of the AHF Lifted index and Showalter index over Utsunomiya with 10-min interval between 2200 UTC 14 July and 0300 UTC 15 July (data missing at 0240 UTC 15 July).

(Fig. 4b), respectively.

KI is less than 25°C (< 40% air mass thunderstorm probability) between 1200 UTC 14 July and 0100 UTC 15 July, and starts increasing at 2100 UTC 14 July, and becomes larger than 26°C (> 40% air mass thunderstorm probability) at 0300 UTC 15 July in Fig. 4c. TT shows increasing trend during this period and becomes larger than 44°C (isolated moderate thunderstorms) at 0400 UTC 15 July in Fig. 4c. The 10-min interval variations of both KI and TT show overall increasing trend in Fig. 4d, although KI is decreased by 4°C in 30 minutes between 0010 UTC and 0040 UTC 15 July and similar change is also observed with TT which is not depicted in the 1-hr frequency. KI becomes larger than 26°C (40-60% air mass thunderstorm probability) at 0230 UTC 15 July and TT increases during this 5-hr period but less than 44°C in Fig. 4d. The variations of KI and TT are similar in this study: their correlation coefficients are 0.79 for the 1-hr interval trend (Fig. 4c) and 0.98 for the 10-min interval trend (Fig. 4d).

CAPE shows increasing trend between 1200 UTC 14 July and 0600 UTC 15 July but is far less than 1000 J kg^{-1} , indicating a weak instability (Figs. 4e and 4f). TPW shows an increasing trend over both 1-hr and 10-min intervals (Figs. 4e and 4f), which provides favorable conditions for the upcoming rainfall. Between 2200 UTC 14 July and 0300 UTC 15 July, TPW increases by 5.5 mm (from 32.2 mm to 37.7 mm). A slight decrease of TPW is also observed during the abrupt changes of the atmospheric stability indices towards the stable atmospheric state between 0000 UTC and 0100 UTC 15 July corresponding to the decrease of the water vapor in the lower troposphere below 700 hPa (Fig. 4f). The changes of the atmospheric stability indices and TPW are well correlated in the 1-hr and the 10-min frequency during the pre-landfall environment of typhoon Nangka favorable for the upcoming

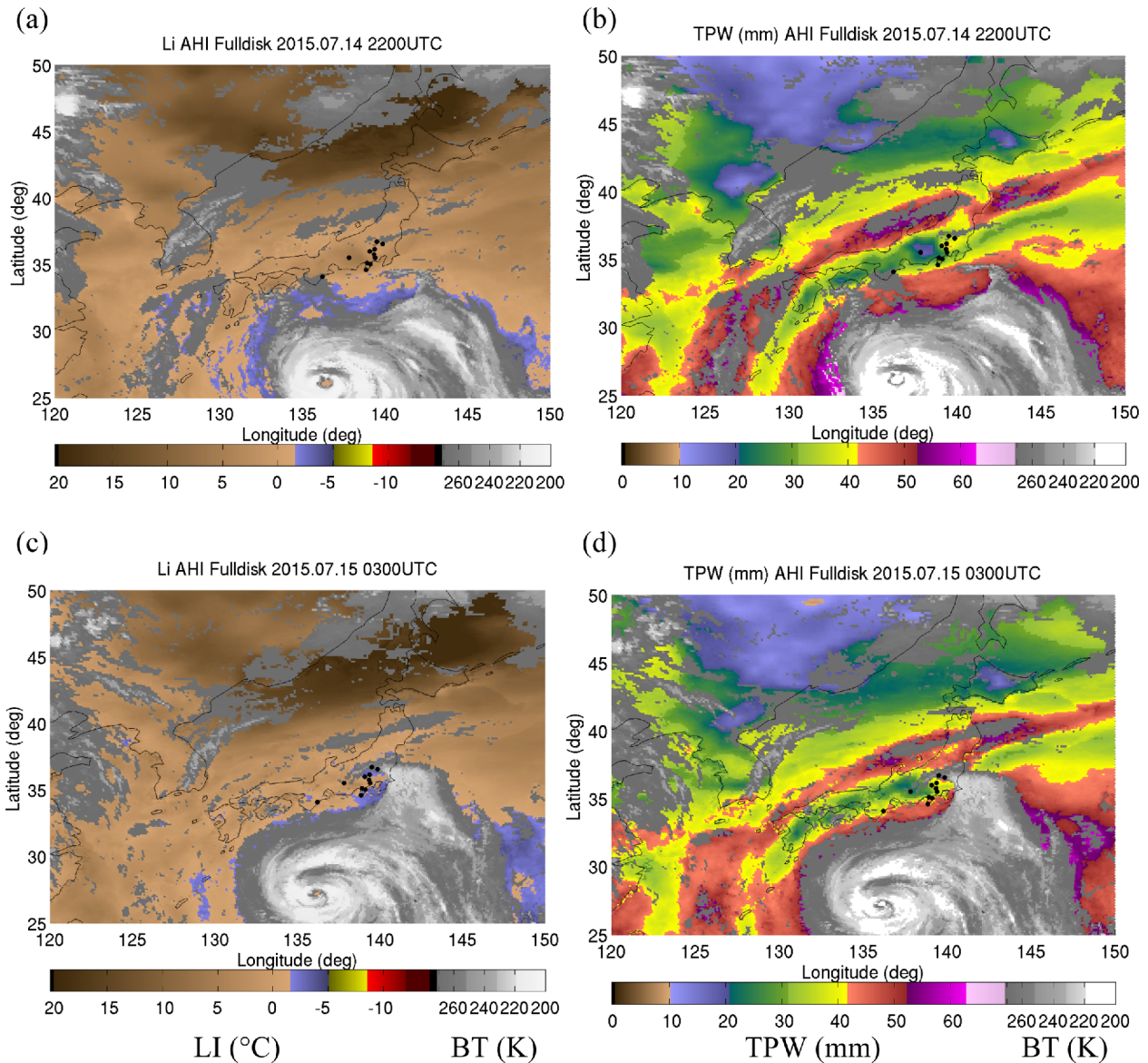


Fig. 6. TPW (Total Precipitable Water) and LI (lifted index) over clear skies with 11 μm brightness temperature in gray valid at 2200 UTC 14 July, 2015 [(a) and (b)] and 0000 UTC 15 July, 2015 [(c) and (d)] (subsetted from the full disk observations). Black dots indicate the selected 11 ISD locations.

heavy rainfall. The correlation coefficients between TPW and each atmospheric stability index are well above than 0.7 in magnitude except the case (-0.61) of 10-min SI.

There are two main benefits for higher time resolution products such as TPW and the stability indices. The first is that it allows for a more smooth transition for monitoring changes, and any changes can be monitored sooner. The second main benefit is that it allows for multiple looks, some of which could be obscured by clouds. Hence the finer time resolution allows obtaining information between cloudy scenes. One example of this case is shown over Utsunomiya in 10-min frequency between 2200 UTC 14 July and 0300 UTC 15 July in Fig. 5. The hourly retrievals are not available due to clouds

between 0000 UTC and 0300 UTC 15 July, while there are two more intermittent retrievals available in the 10-min frequency during this period, which allows providing the forecasters with the information regarding the changing atmospheric state.

The horizontal distributions of TPW and LI valid at 2200 UTC 14 July and 0300 UTC 15 July and the selected 11 ISD locations are shown in Fig. 6. Since all atmospheric stability indices indicate similar feature over the selected 11 ISD locations, LI is chosen for demonstration. The atmospheric state is stable (positive LI) over most of the selected 11 ISD locations at 2200 UTC 14 July, 2015 and become unstable (negative LI), along with the overall TPW increase from 2200

Table 4. Atmospheric stability indices and TPW available from three radiosonde sites neighboring the heavy rainfall areas during 15 and 16 July. Locations of these sites are indicated as “x” in Fig. 1.

	Shionomisaki			Hamamatsu			Tateno		
	14 July		15 July	14 July		15 July	14 July		15 July
	1200 UTC	0000 UTC	1200 UTC	1200 UTC	0000 UTC	1200 UTC	1200 UTC	0000 UTC	1200 UTC
LI (°C)	0.65	-2.08	-1.78	1.22	0.98	0.20	2.21	1.36	0.04
SSI (°C)	7.70	3.47	0.03	4.54	4.22	1.61	4.96	0.98	-0.31
TT (°C)	33.40	40.00	42.40	36.50	39.60	40.70	37.60	41.70	45.40
KI (°C)	17.50	29.10	34.40	20.60	21.50	33.30	26.10	12.20	35.90
CAPE (J kg ⁻¹)	13.30	404.09	220.93	0.00	2.18	18.50	0.00	8.70	0.73
TPW (mm)	30.79	43.32	61.95	38.49	34.19	59.52	38.16	38.96	53.25

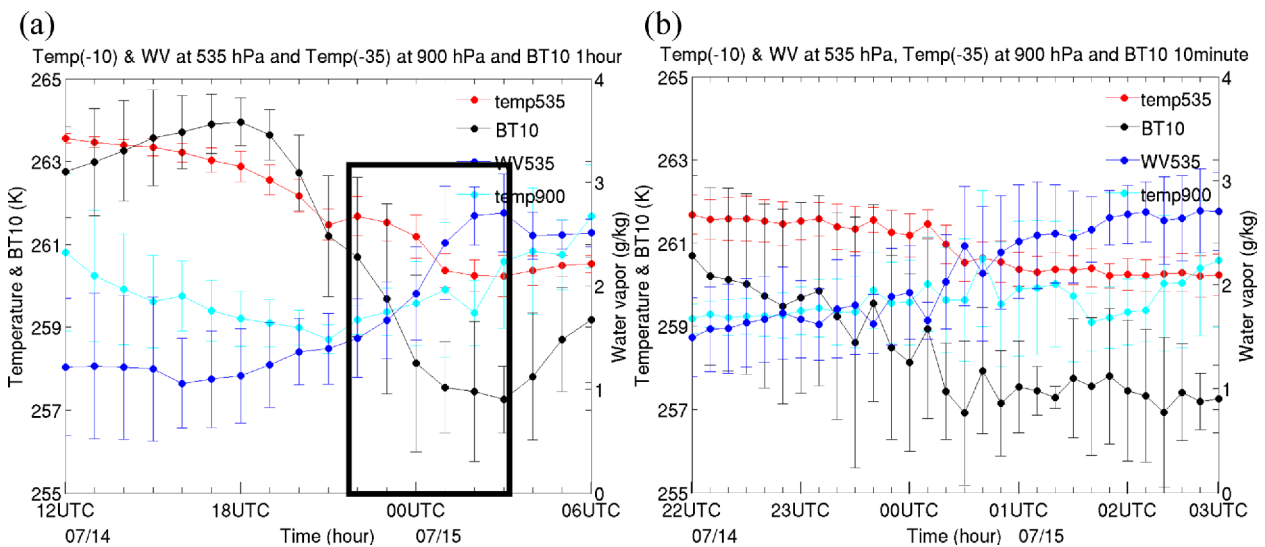


Fig. 7. Time series of the averaged AHI LAP atmospheric temperature and water vapor at 535 hPa, atmospheric temperature at 900 hPa and brightness temperature at band 10 (7.3 μm) over 11 ISD locations in Japan where the accumulated rainfall was over 30 mm in 15 July, 2015 and over 100 mm during two days in 15 and 16 July, 2015: (a) with 1-hr interval between 1200 UTC 14 July and 0600 UTC 15 July and (b) with 10-min interval between 2200 UTC 14 July and 0300 UTC 15 July (data missing at 0240 UTC 15 July). The rectangular box in (a) indicates the 10-min period in (b). The original atmospheric temperature values at 535 hPa and 900 hPa have been subtracted by 10 K and 35 K, respectively, for the convenient comparison with the brightness temperature on the same scale. Vertical bars indicate the standard deviation over the selected 11 ISD locations.

UTC 14 July to 0300 UTC 15 July over the selected 11 ISD locations due to the coming typhoon. The increase of TPW values and the atmospheric instability over selected 11 ISD locations in Figs. 4 and 6 indicate the fast development of a pre-landfall environment favorable for heavy rainfall. Note that the current retrieval being limited to the clear sky pixels, a cloudy sky retrieval would be able to fill up some of the empty (cloudy) area with the atmospheric stability information (Li et al., 2009).

Radiosonde observations can also be used to examine the atmospheric stability. During two days, 14 and 15 July, there are radiosonde observations over three radiosonde sites neighboring the heavy rainfall area and the site locations are indicated in Fig. 1. Table 4 provides the atmospheric stability indices and TPW which are available at these radiosonde sites

(<http://weather.uwyo.edu/upperair/sounding.html>) between 1200 UTC 14 July and 1200 UTC 15 July. Since there is no corresponding radiosonde observation matching the AHI LAP retrievals under clear skies, the comparisons of vertical temperature/moisture profiles between radiosonde observations and AHI LAP retrievals are not included. However, the temporal variation of the atmospheric stability indices and TPW over these sites would be helpful to understand the pre-landfall environment of typhoon Nangka. LI and SI (TT and KI) are decreasing (increasing) over this period indicating that the atmosphere becomes unstable. CAPE shows increasing trend but the magnitude is small, which is similar to the cases in 11 ISD locations. The increasing TPW indicates more moisture is transported into these locations; TPW is increased by more than 15 mm at each radiosonde site in 24 hours.

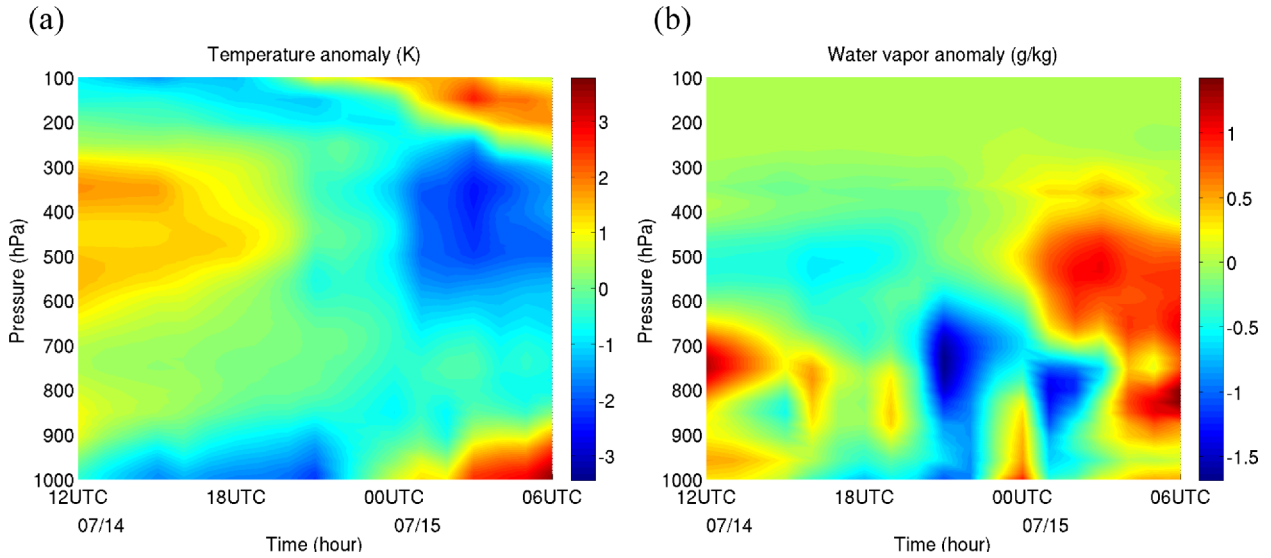


Fig. 8. The temporal sequence of (a) composited temperature (K) and (b) composited water vapor pressure (g kg^{-1}) over 11 ISD locations in Japan where the accumulated rainfall was over 30 mm in 15 July, 2015 and over 100 mm during two days in 15 and 16 July, 2015. The temporal average is calculated for each pressure level during the period between 1200 UTC 14 July and 0600 UTC 15 July and the value at each time subtracted by the temporal average is considered the anomaly.

Overall, the atmospheric environments over three radiosonde sites reveal the similar temporal changes in atmospheric stability and TPW indicated by the hourly variation in Fig. 4. However, radiosonde is not able to tell the detailed trend when the environment starts to change and the rate of the change. Neither is the GFS 3-hr forecast.

The BTs from the water vapor absorption bands are closely related with atmospheric temperature and the amount of water vapor, and it is also interesting to see the variation of these variables in the pre-landfall environment of a typhoon. AHI provides BT measurements in three water vapor absorption bands at 6.25, 6.95, and 7.35 μm (Table 1). These BTs have weighting functions peaking at the high, middle and low vertical level in the middle troposphere (Schmit et al., 2005), respectively, revealing the best water vapor information layers (Di et al., 2016). The two factors, the temperature and the amount of water vapor, affect the BT differently. When there is more water vapor, more outgoing radiance from the surface is absorbed by water vapor and less outgoing radiance is allowed to reach the satellite, and thus the BT is decreased. Meanwhile, the warmer the temperature is, the more the outgoing radiance is. Since the BTs at 6.25, 6.95 and 7.35 μm have similar trend during this period, the BT at 7.35 μm (peaking at around 535 hPa) averaged over 11 ISD locations is shown in Fig. 7. Both the AHI LAP retrieved atmospheric temperature and water vapor at 535 hPa averaged over 11 ISD locations are also depicted in Fig. 7. For the convenience in comparison of atmospheric temperature and BT, atmospheric temperatures at 535 hPa and 900 hPa are subtracted by 10 K and 35 K, respectively, from its original value to fit them on the same scale. The variation of BT at 7.35 μm is well corresponding to the trend of the temperature and the amount of water vapor. The

BT at 7.35 μm increases between 1200 UTC and 1800 UTC 14 July and decreases after that until 0300 UTC 15 July and then slightly increases (Fig. 7a), meanwhile the water vapor at 535 hPa slightly decreases during the first several hours after 1200 UTC 14 July and increases from 1600 UTC 14 July through 0300 UTC 15 July and then slightly decreases after 0300 UTC 15 July. As indicated by the atmospheric temperature at 535 hPa, the atmospheric temperatures in the middle troposphere show decreasing trends in this period, while the atmospheric temperatures below 850 hPa shows increasing trends. This provides a favorable environment for increased instability in the troposphere. The 10-min interval variation in Fig. 7b demonstrates the increase in the water vapor amount at 535 hPa, the decrease in BT at 7.35 μm and the atmospheric temperature at 535 hPa, and the increase in atmospheric temperature in the lower troposphere between 2200 UTC 14 July and 0300 UTC 15 July, which is an indicator for the possible subsequent heavy rainfalls. Again, both the 1-hr and the 10-min interval time series in Fig. 7 show that the increase (decrease) of the water vapor (atmospheric temperature) at 535 hPa is corresponding to the decrease of the BT at 7.35 μm . The correlation coefficients between the BT at 7.35 μm and the atmospheric temperature/water vapor at 535 hPa are 0.94/-0.94 for the hourly measurements and 0.92/-0.91 for the 10-min measurements indicating that the AHI LAP retrieved atmospheric temperature and water vapor well depict the change in the BT measurements. Since the BTs at the three water vapor absorption bands are incorporated in the AHI LAP retrieval, it is reasonable to have corresponding variations in the atmospheric temperature, amount of water vapor, and BTs at these water vapor absorption bands.

Figure 8 shows the temporal (hourly interval) sequence of

temperature and water vapor anomaly over 11 ISD locations during the same period in Figs. 4 and 7. The temperature anomaly shows positive values in the middle troposphere and negative values in the lower troposphere indicating stabilized atmospheric condition before 2200 UTC 14 July, while after this time the atmospheric condition becomes destabilized: negative temperature anomaly in the middle troposphere and positive anomaly in the lower troposphere. The water vapor anomaly also shows positive value emerging in the middle troposphere at around 2200 UTC 14 July and thereafter the positive anomaly gradually extends to the lower troposphere. Both temperature and water vapor variations indicate that a favorable condition builds up rainfall in these locations by developing atmospheric instability and moistening the atmosphere after around 2200 UTC 14 July, which also explains the variations of the atmospheric stability indices and TPW in Fig. 4. These results are similar to Masunaga (2012)'s finding of the temporal sequence of temperature and water vapor anomaly in the subtropical deep convection cases. They found positive (negative) temperature anomaly in the lower and upper (middle) troposphere and also positive water vapor anomaly in the middle and lower troposphere before the deep convection is observed in the subtropical deep convection cases.

4. Summary

AHI onboard Himawari-8 provides radiance measurements at 16 bands. Due to the similarity in the infrared bands between AHI and ABI, the GOES-R ABI LAP retrieval algorithm can be applied to process the AHI measurements with minimal modification. This study reveals the advantages of the high frequency (10 min) measurements of AHI by showing the variation of atmospheric status in pre-landfall environment for typhoon Nangka (2015) over clear skies. Typhoon Nangka made its landfall over Japan at 1407 UTC on 16 July 2015, with significant rainfalls observed over the southern part of Honshu Island well in advance of its landfall. ISD data are used as reference for the precipitation information. 11 ISD stations are selected with the accumulated rainfall more than 30 mm in 15 July and 100 mm in two days of 15 and 16 July. The atmospheric stability indices retrieved from the AHI measurements show steady changes towards the atmospheric instability during the several hours between around 2200 UTC 14 July and 0300 UTC 15 July over these 11 ISD stations. Before this period, all the averaged atmospheric stability indices indicate the atmospheric state is stable or relatively stable. After approximately 0300 UTC 15 July until 0600 UTC 15 July, all the averaged atmospheric stability indices imply greater instability of the atmosphere. The development of the favorable environment for the heavy rainfalls over the south region of Honshu Island during 15 and 16 July, 2015 is indicated by the variations of the atmospheric stability indices and TPW. The development of the favorable conditions for the heavy rainfalls is also indicated by the overall trend of decrease in BT at $7.35 \mu\text{m}$ being well matched with the overall

trend of increase (decrease) in the amount (temperature) of water vapor at 535 hPa between 2200 UTC 14 July and 0300 UTC 15 July. The decrease (and increase) of the atmospheric temperature in the middle (and lower) troposphere and the moistening of the middle and lower troposphere provide favorable conditions for the atmospheric instability. Some details which cannot be detected or are flattened in the hourly measurements are clearly seen in the 10-min frequency measurements. A glimpse to see the atmospheric change within cloud openings, as clouds come and go, is also allowed by the 10-min frequency measurements.

The AHI LAP retrieval algorithm is running in real-time at the Cooperative Institute for Meteorological Satellite Studies (CIMSS) using the AHI full disk measurements and a selected region (including Guam) of the retrieved output has recently been implemented on the NWS's Advanced Weather Interactive Processing System (AWIPS)-II for the weather forecasters and is planned to be assimilated in the CIMSS Regional Assimilation System (CRAS) soon. Although derived vertical profiles and derived parameters from the AHI are shown to be useful in this study, the spectral resolution is limited on these imagers. Improved retrievals would be possible from high-spectral resolution IR measurements, ideally coupled with high time resolution measurements (Schmit et al., 2009).

Acknowledgements. This work was funded by GOES-R algorithm working group (AWG) program under the National Oceanic and Atmospheric Administration Cooperative Agreement NA15NES4320001. The views, opinions, and findings contained in this report are those of the authors and should not be construed as an official National Oceanic and Atmospheric Administration or U.S. Government position, policy, or decision. More information about the AHI from the JMA can be found at: http://www.data.jma.go.jp/mscweb/en/himawari89/space_segment/spsg_ahi.html.

Edited by: Soon-Il An

References

- Bessho, K., and Coauthors, 2016: An introduction to Himawari-8/9 - Japan's new-generation geostationary meteorological satellites. *J. Meteor. Soc. Japan*, **94**, 151-183, doi:10.2151/jmsj.2016-009.
- Chen, Y., Y. Han, P. Van Delst, and F. Weng, 2010: On water vapor Jacobian in fast radiative transfer model. *J. Geophys. Res.*, **115**, D12303, doi:10.1029/2009JD013379.
- _____, _____, and F. Weng, 2012: Comparison of two transmittance algorithms in the Community Radiative Transfer Model: Application to AVHRR. *J. Geophys. Res.*, **117**, D06206, doi:10.1029/2011JD016656.
- Di, D., Y. Ai, J. Li, W. Shi, and N. Lu, 2016: Geostationary satellite-based $6.7 \mu\text{m}$ band best water vapor information layer analysis over the Tibetan Plateau. *J. Geophys. Res.*, **121**, 4600-4613, doi:10.1002/2016-JD024867.
- Houze, R. A., 1993: *Cloud Dynamics*. Academic Press, 573 pp.
- Huntrieser, H., H. H. Schiesser, W. Schmid, and A. Waldvogel, 1997: Comparison of traditional and newly developed thunderstorm indices for Switzerland. *Wea. Forecasting*, **12**, 108-124.

- Jayakrishnan, P. R., and C. A. Babu, 2014: Assessment of convective activity using stability indices as inferred from radiosonde and MODIS data. *Atmos. Climate Sci.*, **4**, 122-130, doi:10.4236/acs.2014.41014.
- Jin, X., J. Li, T. J. Schmit, J. Li, M. D. Goldberg, and J. J. Gurka, 2008: Retrieving clear-sky atmospheric parameters from SEVIRI and ABI infrared radiances. *J. Geophys. Res.*, **113**, D15310, doi:10.1029/2008-JD010040.
- Lee, Y.-K., Z. Li, J. Li, and T. J. Schmit, 2014: Evaluation of the GOES-R ABI LAP retrieval algorithm using the GOES-13 sounder. *J. Atmos. Oceanic Technol.*, **31**, 3-19, doi:10.1175/JTECH-D-13-00028.1.
- Li, J., and Coauthors, 2010: GOES-R Advanced Baseline Imager (ABI) algorithm theoretical basis document for legacy atmospheric moisture profile, legacy atmospheric temperature profile, total precipitable water, and derived atmospheric stability indices. NOAA NESIDIS STAR., 106 pp. [Available online at http://www.goes-r.gov/products/ATBDs/baseline/Sounding_LAP_v2.0_no_color.pdf]
- _____, J. Li, J. Otkin, T. J. Schmit, and C.-Y. Liu, 2011: Warning information in a preconvective environment from the geostationary advanced infrared sounding system - A simulation study using IHOP case. *J. Appl. Meteor. Climatol.*, **50**, 776-783, doi:10.1175/2010-JAMC2441.1.
- _____, C.-Y. Liu, P. Zhang, and T. J. Schmit, 2012: Applications of full spatial resolution space-based advanced infrared soundings in the preconvective environment. *Wea. Forecasting*, **27**, 515-524, doi:10.1175/WAF-D-10-05057.1.
- Li, Z., J. Li, W. P. Menzel, J. P. Nelson III, T. J. Schmit, E. Weisz, and S. A. Ackerman, 2009: Forecasting and nowcasting improvement in cloudy regions with high temporal GOES Sounder infrared radiance measurements. *J. Geophys. Res.*, **114**, D09216, doi:10.1029/2008JD010596.
- Lin, Y.-L., S. Chiao, T.-A. Wang, M. L. Kaplan, and R. P. Weglarz, 2001: Some common ingredients for heavy orographic rainfall. *Wea. Forecasting*, **16**, 633-660.
- Lindsey, D. T., T. J. Schmit, W. M. MacKenzie Jr., C. P. Jewett, M. M. Gunshor, and L. Grasso, 2012: 10.35 μm : An atmospheric window on the GOES-R Advanced Baseline Imager with less moisture attenuation. *J. Appl. Remote Sens.*, **6**, 063598, doi:10.1117/1JRS.6.063598.
- Masunaga, H., 2012: A satellite study of the atmospheric forcing and response to moist convection over tropical and subtropical oceans. *J. Atmos. Sci.*, **69**, 150-167, doi:10.1175/JAS-D-11-016.1.
- Miller, R. C., 1972: Notes on Analysis and Severe-Storm Forecasting Procedures of the Air Force Global Weather Central. Tech. Report 200(R), 190 pp.
- Padula, F. P., and C. Cao, 2014: Using S-NPP VIIRS as a transfer radiometer to inter-compare GOES-R ABI and Himawari-8 AHI. *Extended Abstract, 94th AMS Annual meeting*, Atlanta. [Available online at <https://ams.confex.com/ams/94Annual/webprogram/Paper-235594.html>]
- Schmit, T. J., M. M. Gunshor, W. P. Menzel, J. J. Gurka, J. Li, and S. Bachmeier, 2005: Introducing the next-generation advanced baseline imager (ABI) on GOES-R. *Bull. Amer. Meteor. Soc.*, **86**, 1079-1096, doi:10.1175/BAMS-86-8-1079.
- _____, J. Li, J. L. Li, W. F. Feltz, J. J. Gurka, M. D. Goldberg, and K. J. Schrab, 2008: The GOES-R Advanced Baseline Imager and the continuation of current sounder products. *J. Appl. Meteor. Climatol.*, **47**, 2696-2711, doi:10.1175/2008JAMC18581.
- _____, J. Li, S. A. Ackerman, and J. J. Gurka, 2009: High-spectral- and high-temporal-resolution infrared measurements from geostationary orbit. *J. Atmos. Oceanic Technol.*, **26**, 2273-2292.
- _____, and Coauthors, 2013: Geostationary Operational Environmental Satellite (GOES)-14 super rapid scan operations to prepare for GOES-R. *J. Appl. Remote Sens.*, **7**, 073462, doi:10.1117/1.JRS.7.073462.
- _____, and Coauthors, 2015: Rapid refresh information of significant events: Preparing users for the next generation of Geostationary Operational Satellites. *Bull. Amer. Meteor. Soc.*, **96**, 561-576, doi:10.1175/BAMS-D-13-00210.1.
- _____, P. Griffith, M. M. Gunshor, J. M. Daniels, S. J. Goodman, and W. J. Lebar, 2017: A Closer Look at the ABI on the GOES-R Series. *Bull. Amer. Meteor. Soc.*, **98**, 681-698, doi:10.1175/BAMS-D-15-00230.1.
- Seemann, S. W., J. Li, W. P. Menzel, and L. E. Gumley, 2003: Operational retrieval of atmospheric temperature, moisture, and ozone from MODIS infrared radiances. *J. Appl. Meteorol.*, **42**, 1072-1091, doi:10.1175/1520-0450(2003)042<1072:OROATM>2.0.CO;2.
- _____, E. E. Borbas, R. O. Knuteson, G. R. Stephenson, and H.-L. Huang, 2008: Development of a global infrared land surface emissivity database for application to clear sky sounding retrievals from multi-spectral satellite radiance measurements. *J. Appl. Meteor. Climatol.*, **47**, 108-203, doi:10.1175/2007JAMC1590.1.
- Weng, F., Y. Han, P. van Delst, Q. Liu, T. Kleespies, B. Yan, and J. Le Marshall, 2005: JCSDA community radiative transfer model (CRTM). *Proc. 14th International ATOVS Study Conference*, Beijing, 217-222.